Enhanced thermoelectric properties of two-dimensional Janus ferromagnetic LaBrI with strain-induced valley degeneracy

Anuja Kumari,[1,*] Raman D. K.,[2] Tanu Choudhary,[3] Raju K. Biswas,[3,4] Abhinav Nag,[5]
Santanu K. Maiti,[1,†] and Jagdish Kumar[2]
[1]*Physics and Applied Mathematics Unit, Indian Statistical Institute, 203 Barrackpore Trunk Road, Kolkata- 700 108, India*
[2]*Department of Computational Sciences, Central University of Punjab, Bathinda-151 401, India*
[3]*Department of Physics, M S Ramaiah University of Applied Sciences, Bengaluru-560 058, India*
[4]*Department of Physics, North Eastern Regional Institute of Science and Technology, Nirjuli, Arunachal Pradesh-791 109, India*
[5]*Department of Physics, GGDSD College, Rajpur, Palampur-176 061, India*

(Received 10 January 2024; revised 5 March 2025; accepted 1 April 2025; published 22 April 2025)

Since the successful synthesis of the MoSSe monolayer, which violated the out-of-plane mirror symmetry of transition metal dichalcogenide monolayers, considerable and systematic research has been conducted on Janus monolayer materials. By systematically analyzing the LaBrI monolayer, we are able to learn more about the novel Janus material by focusing on the halogen family next to group VIA (S, Se, Te). The structural optimizations have been carried out using pseudopotential-based Quantum Espresso code. Computed structural parameters are in good agreement with literature reports. The optimized crystal structures are used for computing the effect of strain on electronic and thermoelectric properties. Dynamical stability predicts that this material can withstand up to 10% of tensile strain. Computed electronic structure reveals material to be indirect wide band-gap ferromagnet with magnetic moment 1 μ_B. With increase in the biaxial tensile strain the band gap decreases. Furthermore, the computed magnetothermoelectric properties predict high Seebeck coefficient ~400 μV/K and low thermal conductivity of ~0.93 W/m K in LaBrI, which results in a high *ZT*~1.84 for 4% strain at 800 K. The present study supports the fact that tensile strain on ferromagnetic LaBrI material can further enhance TE properties, making it a promising material for TE applications at higher temperatures.

DOI: 10.1103/PhysRevB.111.155433

I. INTRODUCTION

Clean energy sources and renewable energy technology are the utmost priority of scientists, ecologists, and researchers to combat global warming and climate change [1–5]. Among various factors, waste heat is one of the prime concerns causing this. By scavenging wasted heat, we can save energy and promote efficient energy production [6–11]. Thus, it is significant to explore new ways to generate, convert, and store energy. Thermoelectric generators (TEGs) are a highly effective solution in managing waste heat as they can convert waste thermal heat into useful electrical energy [12–16]. TEGs are significantly known for their applications in deep-space exploration because of immobile parts, silent working, and steadiness during years of operation. A thermoelectric module is simply composed of parallel thermal and series electrical connections between pairs of highly doped *p*-type and *n*-type semiconductors. For any good TE module, these *p*-type and *n*-type TE materials are crucial. Thus, researchers have explored many different TE materials for power generation at various temperatures. However, conversion efficiency is not yet achieved for commercialization of this technology and is yet a challenge [17–20]. The efficiency of any thermoelectric material is assessed by a dimensionless parameter called a figure of merit, denoted by *ZT,* as [21,22]

$$ZT = \frac{S^2\sigma T}{\kappa_e + \kappa_l}. \tag{1.1}$$

In the above equation, S represents the Seebeck coefficient, σ represents the electrical conductivity, κ_e represents electronic- and κ_l represents phononic thermal conductivity. Thus, a factor known as the power factor, $S^2\sigma$, indicates the electric performance of the material. To achieve optimal thermal performance at a certain temperature, a higher power factor and lower thermal conductivity are desirable [23–26]. However, for any given material three parameters S, σ, and κ_e are coupled together, and optimizing them simultaneously is a daunting task [27–32]. This unveils various strategies to improve TE materials such as power-factor augmentation by carrier filtering [33–37], carrier pocket engineering [38–40], complex structures [41,42], low-dimensional structures [43–45], valley degeneracy [46], etc. that improve *ZT* significantly. Also, improved phonon scattering using nanostructuring has been used to raise the TE material's energy conversion efficiency [47].

With the prediction of excellent transport properties and large power factors of graphene [48] and other materials [49–52], many layered materials have been investigated for thermoelectric applications. Due to their unique structural, physical, and chemical properties and easy synthesis using a

---

[*] Contact author: anudhiman45@gmail.com

[†] Contact author: santanu.maiti@isical.ac.in

variety of methods such as chemical vapor deposition, physical vapor deposition, mechanical exfoliation, etc., they are of recent interest in thermoelectrics [53–56]. Gu and Yang [57] predicted that altering the stoichiometry of the structure can lead to a significant reduction in the lattice thermal conductivity. The *ZT* can be efficiently increased by lowering the lattice thermal conductivity. Recently, the synthesis of Janus MoSSe monolayer [58] inspired the research community to explore a new family of 2D materials named Janus materials. Due to highly asymmetric structural characteristics, Janus materials exhibit diverse properties, including finite out-of-plane dipoles, giant Rashba splitting, a wide range of direct and indirect band gaps, etc. [58]. In Janus transition-metal dichalcogenide monolayer, the layer of metal atoms is sandwiched between two layers of dissimilar chalcogen atoms. They possess an extra degree of freedom to tune material properties while retaining the exotic characteristics of their parent structure. Numerous works in the literature suggested that these Janus materials could be a potential material for TE applications [52]. Furthermore, recent theoretical studies suggested that the Janus monolayer could be useful in a variety of emerging fields [59]. For thermoelectric application, study by Abhishek *et al.* [60] reported a high *ZT* of 2.56 for the WSTe Janus monolayer at higher temperature; another Janus monolayer ZrSSe studied by Zhao *et al.* [61] provided a high *ZT* of 4.41 and 4.88, respectively, for *p*-type and *n*-type materials with a tensile strain of 6%. Similarly, *ZT* of 2.54 for PtSeTe Janus monolayer was observed at 900 K by Wang *et al.* [62] and $ZT\sim3.00$ was reported by Shivani *et al.* [63] in MoSSe Janus monolayer at 1200 K.

Magnetic Janus materials have also been proposed recently such as manganese chalcogenides [64] and chromium trihalides [65]. Jiang and Kang predicted a 2D magnetic Janus ferrovalley material LaBrI to be a stable ferromagnetic electrode [66] by employing first-principles investigations. They proposed that the intrinsic magnetism and asymmetric nature of these materials result in a large valley degeneracy, hence making these materials a promising choice for various applications. Interestingly, due to valley degeneracy, the WSSe Janus monolayer shows good thermoelectric properties [67]. Motivated by their idea, we have investigated various properties of 2D magnetic Janus material LaBrI for thermoelectric applications. Janus monolayer of LaBrI has broken out-of-plane symmetry from D_{3h} ($LaBr_2$) to C_{3V} (LaBrI) with space group *P3m1* (No. 156) as shown in Fig. 1. This monolayer is a three-atom-thick layered structure with La atoms sandwiched between two halogen atoms Br and I having reflection asymmetry on the mirror plane.

In the present study, we have systematically investigated the structural properties, dynamical stability, and electronic and thermoelectric properties of this material. Furthermore, we present modulated ferrovalley for up-spin and down-spin charge carriers in electronic band structure that enhances with increase in strain. Due to this modulation in valley degeneracy, low thermal conductivity is observed, which enhances the figure of merit *ZT* to be more than 1. Thermoelectric coefficients as a function of chemical potential at various temperatures predict $ZT>1$ for *p*-type and *n*-type dopings at different temperatures. Obtained low thermal conductivity and high-*ZT* values tuned with strain are the essential findings of our study, which predicts this to be an efficient thermoelectric material.

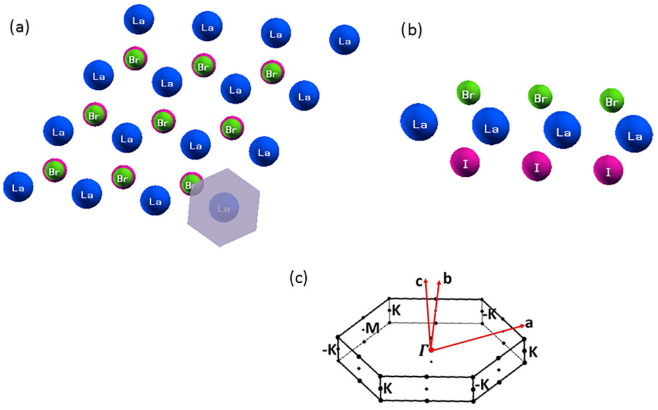

FIG. 1. Crystal structure of 2D Janus monolayer of LaBrI ($P3m1$: No. 156) (a) top view; (b) side view; and (c) Brillouin zone with high-symmetry points.

The present paper is arranged as follows. In Sec. II we discuss the theoretical formalism of density-functional theory (DFT) used in computing all the calculations. In Sec. III we further present and discuss lattice parameters, dynamical stability based on phonon dispersion curves, and various thermoelectric parameters such as the Seebeck coefficient, electrical conductivity, power factor, thermal conductivity, and *ZT* of the material. Finally, in Sec. IV, we conclude with significant outcomes of the present study.

II. COMPUTATIONAL DETAILS

All the calculations were carried out in the framework of the density-functional theory (DFT). Janus monolayer of LaBrI is designed from pristine $LaBr_2$ monolayer by replacing Br atoms with iodine atoms. With the optimized lattice parameters of LaBrI, the calculations of electronic and dynamical properties have been carried out by employing pseudopotential-based Quantum Espresso package [68]. The exchange and correlation interaction among the electrons are described using the nonempirical *generalized gradient approximation* (GGA) within the framework of the PBE (Perdew-Burke-Ernzerhof) formalism, which performs reasonably accurately for a wide range of materials [69]. The charge density and wave-function cutoff were set to 320 and 40 Ry, respectively, throughout the calculations. All calculations were performed using norm-conserving scalar relativistic and fully relativistic pseudopotentials. Due to the presence of heavy elements, spin-orbit coupling (SOC) effect was incorporated using fully relativistic norm-conserving pseudopotentials for all three atoms. We have used a Monkhorst-Pack of $12\times12\times2$ k-point grid for electronic properties and $36\times36\times2$ for thermoelectric properties for sampling the Brillouin zone (BZ). The lattice parameters and atomic positions were obtained by relaxing the structures to force tolerance of 10^{-4} Ry/bohr. A large vacuum space of 15 Å was used along the z axis to prevent any artificial interactions between periodic images of slabs along the vertical direction. The phonon dispersion calculations were employed for the accessing dynamical stability. We obtained the phonon dispersion with a q mesh of $3 \times 3 \times 1$ with a strict convergence threshold of 10^{-10} Ry in the self-consistent calculation using density-functional perturbation theory. The thermoelectric coefficients were computed using the semiclassical Boltzmann transport theory within constant scattering time approximation (CSTA) and the rigid-band approximations, as implemented in the BoltzTraP code [70]. To compute the electronic part of thermal conductivity, the constant value of relaxation time is utilized in BoltzTraP code.

According to semiclassical Boltzmann transport theory, once we get the first-principles band-structure calculations we can define *energy-projected conductivity tensor "$\Theta(\varepsilon)$"* in terms of conductivity tensor as [70]

$$\Theta(\varepsilon) = \frac{1}{N}\sum_{k}\sigma(k)\left(-\frac{\delta(\varepsilon-\varepsilon_k)}{d\varepsilon}\right). \tag{2.1}$$

It shows the distribution in energy and represents the contribution of electrons having a specific energy "ε," and "N" represents the number of k points sampled in the BZ. For a unit-cell crystal having volume Ω, the transport coefficients can be evaluated by integrating this conductivity distribution as

$$\sigma(T,\mu) = \frac{1}{\Omega}\int \Theta(\varepsilon)\left[-\frac{\delta f_\mu(T,\varepsilon)}{\delta k}\right]d\varepsilon, \tag{2.2}$$

$$\kappa_e(T,\mu) = \frac{1}{eT\Omega}\int \Theta(\varepsilon)(\varepsilon-\mu)^2\left[-\frac{\delta f_\mu(T,\varepsilon)}{\delta k}\right]d\varepsilon, \tag{2.3}$$

$$S(T,\mu) = \frac{1}{eT\Omega\sigma(T,\mu)}\int \Theta(\varepsilon)(\varepsilon-\mu)\left[-\frac{\delta f_\mu(T,\varepsilon)}{\delta k}\right]d\varepsilon, \tag{2.4}$$

where T is the equilibrium temperature, μ is the chemical potential, κ_e is the electronic part of the thermal conductivity, and S refers to the Seebeck coefficient.

We have also computed lattice thermal conductivity κ_l by solving the Boltzmann transport equation (BTE) under relaxation-time approximation (RTA). At thermal equilibrium, the phononic distribution obeys Bose-Einstein statistics [71,72]. In the steady state, the phonon distribution function is expressed as

$$\frac{df_\lambda}{dt} = \frac{df_\lambda}{dt}\,|_{\text{diffusion}} + \frac{df_\lambda}{dt}\,|_{\text{scattering}} = 0, \tag{2.5}$$

where f, t, and λ are the distribution function, time, and phonon mode, respectively. The phononic distribution f_λ of two- and three-phonon scattering process is modeled under RTA, where third-order anharmonic force constants are computed to obtain the three-phonon scattering rate. The final lattice thermal conductivity tensor is expressed as

$$k_{\alpha\beta} = \frac{1}{k_B T^2 \Omega N}\sum_{\lambda} f_0(f_0+1)(\hbar\omega_\lambda)^2 \nu_\lambda^\alpha F_\lambda^\beta, \tag{2.6}$$

where Ω, f_0, ν_λ, and N are the volume of the unit cell, equilibrium Bose-Einstein distribution function, group velocities of phonon mode, and the number of q points in the Brillouin zone, respectively.

The lattice thermal conductivity calculations were performed using the phono3py code [73]. The second- and third-order force constants were calculated by using $2 \times 2 \times 1$ supercells, which required force calculations for 333 number of crystal structures containing 12 atoms. The Quantum Espresso code was utilized to perform static calculations. The k-grid size was set to $5 \times 5 \times 1$. The kinetic-energy cutoff for wave functions was set to 50 Ry and the force and energy threshold were set to 10^{-5} Ry/bohr and 10^{-6} Ry, respectively, using phono3py. A well-converged q-mesh size of $20 \times 20 \times 1$, as shown in Fig. S1 (see Supplemental Material [74]), was chosen for calculating thermal conductivity tensors under BTE-RTA (relaxation-time approximation). The calculated lattice thermal conductivity results were then scaled to make it independent of the vacuum thickness. The values were multiplied by the factor of L/d, where L is the length of the z axis and d is the sum of the layer thickness and the van der Waals radii of the outermost atoms.

Finally, the figure of merit (ZT) can be obtained by

$$ZT = \frac{S^2\sigma T}{\kappa_e + \kappa_l}. \tag{2.7}$$

Here, ZT is related to thermal-to-electrical energy-conversion efficiency of any material. To obtain more accurate value of ZT, phononic thermal conductivity plays a significant role and literature suggests that strain-mediated valley degeneracy reduces thermal conductivity significantly [67]. Thus, systematic study of TE properties of Janus monolayer is presented in this paper.

III. NUMERICAL RESULTS AND DISCUSSION

A. Structural properties

By allowing the crystal to relax to a force tolerance of 10^{-4} Ry/bohr, the equilibrium lattice parameters for all the compositions under investigation have been determined. Using the GGA-PBE as the exchange-correlation, we have calculated the lattice constants and other related parameters, which are listed in Table I. The values agree well with the previous reports in literature [66].

B. Lattice dynamics and dynamical stability

The thermoelectric performance of a material drastically changes with the implication of strain (ε). The tensile strain is defined as $\varepsilon\% = (\frac{a-a_0}{a_0}) \times 100$, where a_0 is the equilibrium relaxed lattice constant. We examined the effect of biaxial tensile strain on the dynamical stability of LaBrI by calculating phonon dispersion curves at the steps of $\Delta\varepsilon = 4\%$. Figure 2 illustrates the phonon dispersions at various strains for LaBrI Janus monolayers along different high-symmetry directions.

The computed phonon dispersion for LaBrI comprises three acoustic and six optical branches in the dispersion curves, which is due to the 1 La atom, 1 Br atom, and 1 I atom in the unit cell. The phonon dispersion curves relate the dependence of phonon frequencies for all branches along a selected high-symmetry path (see Supplemental Material [74]). The dynamical stability of a material is associated with the real and imaginary frequencies of the phonon dispersion curves. Any imaginary frequency in the phonon dispersion curve signifies the nonrestorative force that results in the lowering of potential energy of the atoms when displaced from

TABLE I. Variation in band gap with different strain on Janus LaBrI system obtained using GGA-PBE exchange and correlation. Computed energy splitting due to spin-orbit coupling at K and $-K$ high-symmetry points.

S. No.	Biaxial tensile strain(%)	Parameter	LaBrI	Energy splitting (meV)
1	0	Lattice constant (Å)	4.24 (4.24) [66]	
		Band gap (eV)	2.44 eV (↑spin) 1.16 eV (↓spin)	28
2	4	Band gap (eV)	2.75 eV (↑spin) 0.45 eV (↓spin)	49
3	8	Band gap (eV)	3.17 eV (↑spin) 0.14 eV (↓spin)	61
4	10	Band gap (eV)	3.20 eV (↑spin) 0.08 eV (↓spin)	69

equilibrium positions, indicating dynamical instability of the structure. Computed phonon dispersion curves for LaBrI do not contain any imaginary phonon frequencies up to 10%. This indicates that LaBrI monolayer is dynamically stable under tensile strain up to 10%. Further increase in the strain lead to imaginary frequencies in the phonon dispersion curve; hence, material gets unstable beyond this limit.

C. Electronic properties

The spin-polarized electronic band structures for the studied monolayer under various strain values are shown in Fig. 3. Band structures highlight that GGA-PBE predicts LaBrI to be a semiconductor with an indirect band gap of 0.51 eV. Due to spin polarization, valence-band maximum (VBM) and conduction-band minimum (CBM) near the Fermi level possess opposite spin that makes this monolayer a spin semiconductor. It can be seen from Fig. 3 that near Fermi level the bands have local minima for up spin and down spin which are significant and referred to as valleys. These valleys offer additional degree of freedom for the electron along with its charge and spin. With an increase in strain, the electronic valley degree of freedom can be manipulated and hence it can be used to tune the energies of these valleys. LaBrI is a ferromagnetic material with a magnetic moment per unit cell of $\sim 1\mu_B$ [66]. The magnetism is localized in the interstitial region of La atoms. Most contribution of magnetic moment comes from La atoms, while it is negligible at Br and I atomic sites.

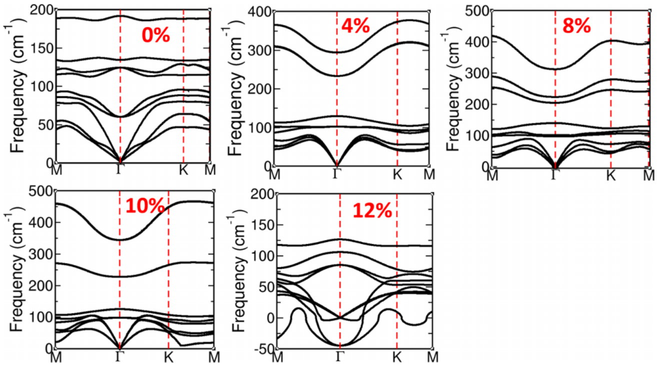

FIG. 2. Phonon dispersion for LaBrI at different biaxial tensile strain along high-symmetry q points.

It is apparent from Fig. 3 that LaBrI shows an indirect band gap from Γ to M point in the BZ. The striking feature in the band structure is the presence of valley polarization at K and $-K$ high-symmetry points. In Janus materials the broken symmetry of the crystal leads to the formation of such valleys that create an additional degree of freedom for tuning the electronic properties. With increase in strain these valleys can be polarized further as they shift closer to the Fermi level. We observed significant changes in the conduction-band region when a tensile strain is applied to the monolayer. The states at both the Γ and M points increase as the strain increases and the states at Γ point shift at a slower rate than those at M point. Moreover, with the increase in tensile strain the band gap decreases. Such decrease in the band gap can be related to the increased bond length with tensile strain leading to reduction in the coupling and energy-band splitting. We found that when a biaxial strain is applied, the band valleys in the Janus monolayer can be significantly tuned. Such tuning of bands due to strain has a significant effect on the band curvatures; hence, the effective mass of the charge carriers

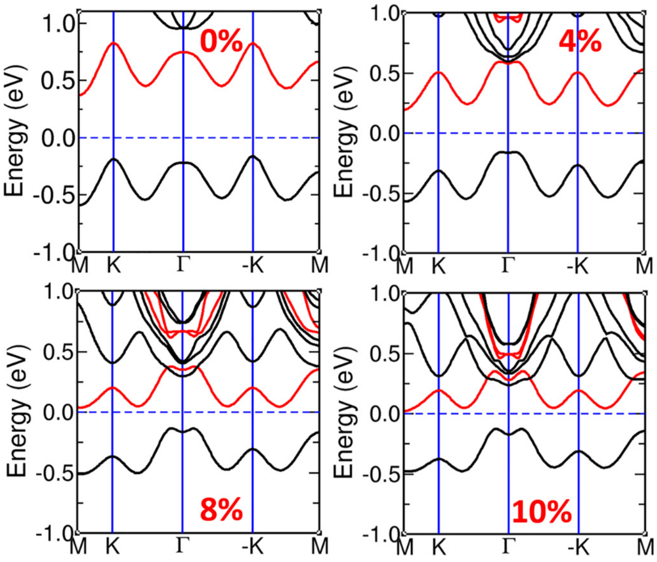

FIG. 3. Electronic band structure showing up spin (black color) and down spin (red color) obtained using GGA-PBE functional for various strains on LaBrI.

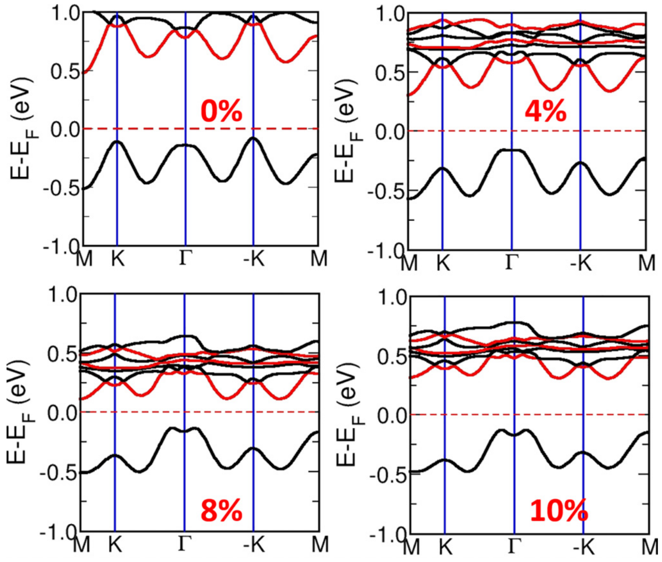

FIG. 4. Electronic band structure showing up spin (black color) and down spin (red color) obtained using GGA+SOC for different strain.

in valence- and conduction bands and hence the transport properties.

The studied Janus layer has heavy atoms such as La and I, which have significant contribution of the spin-orbit coupling on the band structure. Therefore, we have also investigated the effect of SOC+GGA on electronic and transport properties. With the application of SOC there is no significant change observed in the band structure for both unstrained and strained systems. For strained system, the SOC exhibits symmetric band curvatures resulting in insignificant effect on the transport properties of these monolayers. The inclusion of SOC with an initial splitting in the magnetic moment leads to the energy splitting, which depends upon the direction of the magnetization. Due to the magnetization along the $-z$ axis, the obtained energy-band maximum at $-K$ is 28 meV higher than the energy-band maximum at K point for unstrained system as shown in Fig. 4.

Without SOC these energy bands at K and $-K$ are energetically degenerate, showing valley polarization. Further increase in strain with SOC leads to increase in the energy splitting as tabulated in Table I.

The SOC is significantly higher in heavier systems as compared to lighter systems, which leads to the strong band splitting in VBM and CBM resulting in decreasing band gap with strain. Such strong SOC in Janus monolayers and tunable Fermi level with strain or applied field can be a good strategy for tailoring these materials for valleytronics and spintronics applications.

D. Thermoelectric properties

The thermoelectric coefficients of the considered monolayer have been computed, which include the Seebeck coefficient (S), electrical conductivity (σ), electronic part of thermal conductivity (κ_e), and power factor ($S^2\sigma$) by solving the Boltzmann transport equations within constant scattering time approximation (CSTA) and rigid-band assumption. We have investigated the impact of doping the charge carriers on the transport coefficients by varying the chemical potential (μ). The transport properties are dependent significantly on the location of the chemical potential. The negative and positive doping levels of the chemical potential refer to hole (p-type) and electron (n-type) dopings, respectively.

1. *Seebeck coefficient (S)*

The Seebeck coefficient is the induced electric potential due to thermal gradient across a thermocouple. Therefore, a higher Seebeck coefficient signifies higher electric potential across thermal gradient and is essential for higher *ZT* or good thermoelectric material. For a given material, the Seebeck coefficient is related to carrier concentration "n" as [72]

$$S = \frac{8\pi^2 k_B^2 T}{3eh^2} m^* \left(\frac{\pi}{3n}\right)^{2/3}, \tag{3.1}$$

where T is temperature, k_B is Boltzmann constant, e is electronic charge, m^* is effective mass, and h is Planck's constant. Within CSTA, the electronic conductivity tensor $\Theta(\varepsilon)$ using Eq. (2.1), as discussed in Sec. II, can be obtained only from the velocities that follow from electronic band structure. The chemical potential μ is used as a variable parameter to study the effect of doping. The obtained Seebeck coefficient for the monolayer of LaBrI as a function of carrier concentration is depicted in Fig. 5. Seebeck coefficient is directly proportional to the effective mass of the carrier and inversely proportional to the carrier concentration near the Fermi level. For unstrained monolayer, the highest Seebeck coefficient of ~466 μV/K is obtained at 600 K for up-spin charge carriers, which is evident from the band curvatures shown in Fig. 5, as near the Fermi level heavy holes with higher effective mass and low carrier density lead to high Seebeck coefficient. However, for down-spin charge carriers, temperature does not have a significant effect and a coefficient of ~112 μV/K is recorded with positive-doping levels. The Seebeck coefficients for different biaxial tensile strains at various temperatures 600, 800, and 1200 K are also illustrated in these plots. For spin-up charge carriers Seebeck coefficient decreases to ~330 μV/K with strain due to contribution of light holes which have low effective mass and higher carrier concentration. Similar trends are observed with an increase in temperature. However, for down-spin charge carriers, the Seebeck coefficient increases to ~480 μV/K with positive-doping levels at 600 K. At higher temperatures, 800 and 1200 K, we get a significantly low value of the Seebeck coefficients.

2. *Power factor ($S^2\sigma$)*

The *ZT* of any TE material is directly proportional to its power factor (PF), which is defined as $PF = S^2\sigma$. It significantly comprises the electronic conductivity and Seebeck coefficient.

Figure 6 illustrates the calculated power factor as a function of chemical potential employed at different strain under various temperatures. For unstrained LaBrI, spin-up charge carriers show increase in PF from $\sim 1.28 \times 10^{11}$ W/m K at 600 K to $\sim 1.34 \times$ W/m K at 1200 K; spin-down charge carriers show increase in PF from $\sim 1.78 \times 10^{11}$ W/m K at 600 K to $\sim 1.96 \times 10^{11}$ W/m K at 800 K. Further, at

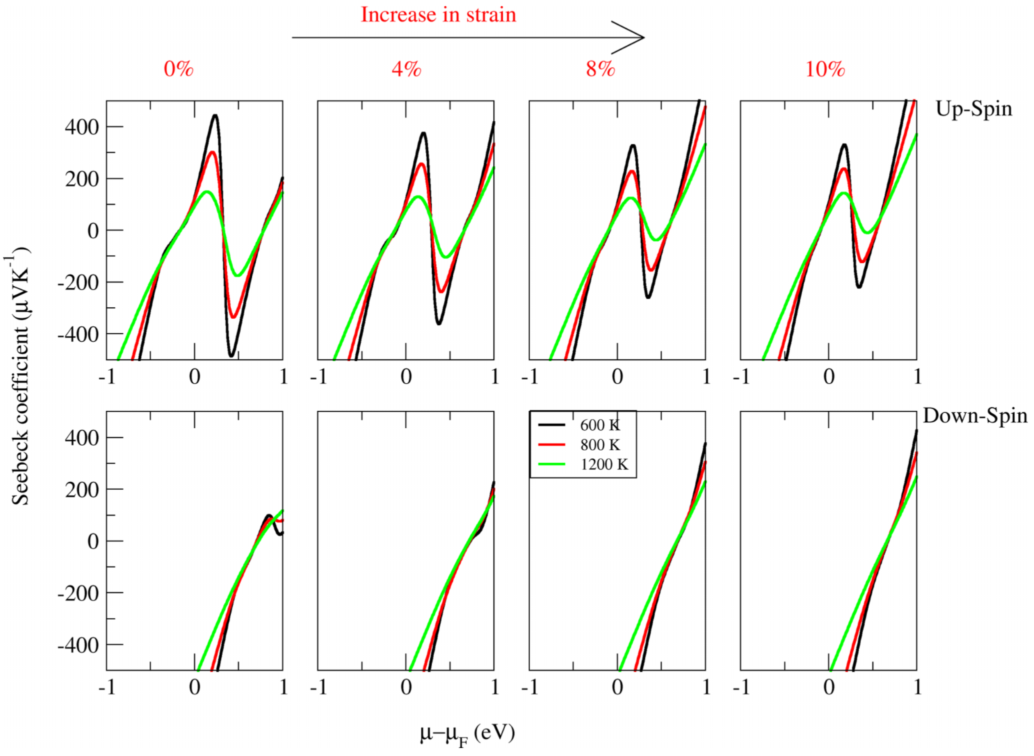

FIG. 5. Seebeck coefficient as a function of chemical potential at 600, 800, and 1200 K for spin-up and spin-down charge carriers.

800 K with 8% strain, spin-up carriers shows PF ~ 1.83×10^{11} W/m K with *p*-type doping and spin-down charge carriers show lower PF ~ 1.04×10^{11} W/m K with *n*-type doping. At high temperatures, we can observe decrease in the power factor. Thus, strain significantly modifies the band curvatures, yielding changes in effective mass of the charge carriers ultimately leading to changes in power factor. High band curvatures for up spin near Fermi level show light holes with

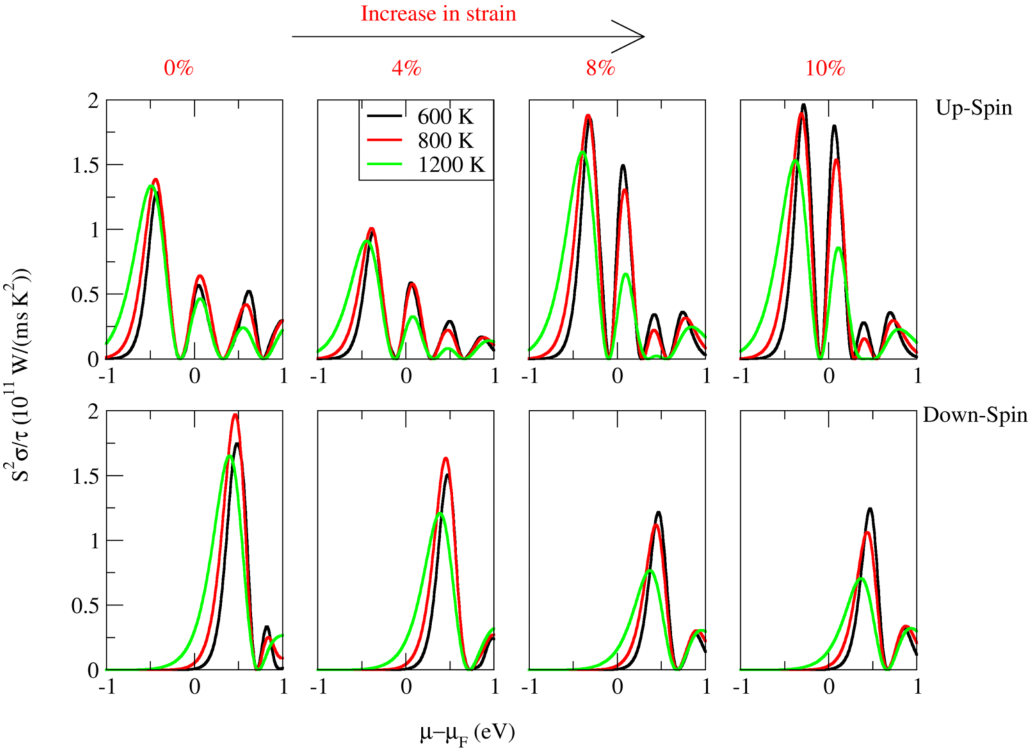

FIG. 6. Spin-resolved power factor as a function of chemical potential at 600, 800, and 1200 K.

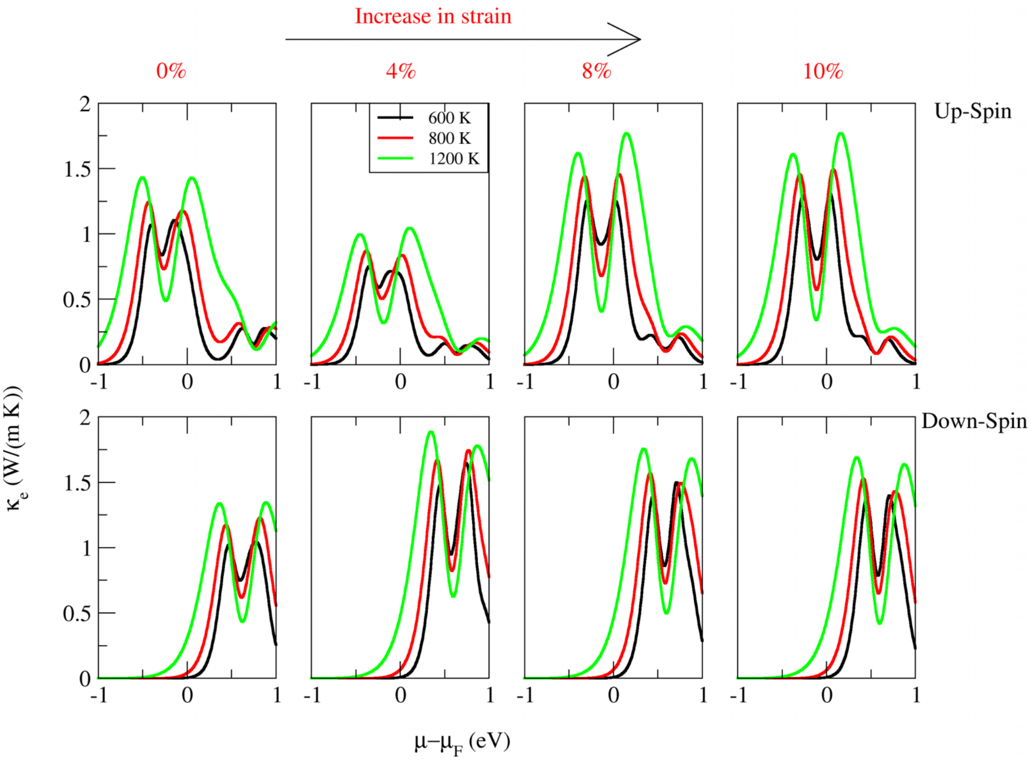

FIG. 7. Variation of electronic part of thermal conductivity with chemical potential at various temperature for up-spin and down-spin charge carriers. Here, κ_e is scaled using relaxation time $\tau = 10^{-14}$ s and for $\tau = 10^{-13}$ s the values will be scaled by multiplying a factor of 10.

less effective mass, which result in high power factor for unstrained system. With increase in strain the band curvatures decrease, resulting in heavy holes with high effective masses; hence, the relevant effect can be seen in the power factor for up-spin and down-spin charge carriers.

3. Thermal conductivity

Thermal conductivity of a material is a sum of electronic thermal conductivity (κ_e) and lattice thermal conductivity (κ_l). Solving Boltzmann transport equations, we have obtained electronic thermal conductivity κ_e. To obtain an optimization between electronic conductivity (σ) and electronic thermal conductivity (κ_e), we need to understand the relation between them. At an absolute temperature, they are related by Wiedemann-Franz law as $\frac{\kappa_e}{\sigma} = LT$ [75,76], where (κ_e) is the electronic thermal conductivity, (σ) is the electrical conductivity, L is the Lorenz number, and T is the absolute temperature. According to this law, which refers to the simplest free-electron model, the electrical and thermal conductivities should be in direct relation to get the Lorenz number as a constant at a particular temperature. However, in a more realistic scenario of complex interactions within the crystal structure, we can find a way to optimize the thermoelectric performance of any material.

Figure 7 depicts the electronic thermal conductivity of this monolayer for n- and p-type dopings at different temperatures. It can be observed from the plots that in an unstrained system, the spin-up and spin-down charge carriers have a lower electronic thermal conductivity of ~ 1.14 and ~ 1.02 W/m K at 600 K, respectively. However, the increase in strain has prominent changes in both spin-up and spin-down charge carriers as, with 4% strain, the thermal conductivity decreases to ~ 0.62 W/m K for spin up and it increases to ~ 1.64 W/m K for spin-down charge carriers at 600 K. A similar trend is observed concerning increase in temperature, respectively. With increase in strain to 4%, electronic thermal conductivity decreases for spin-up and increases for spin-down charge carriers. Therefore, overall the tensile strain seems to be favorable for enhancing the thermoelectric performance of this monolayer.

For good efficiency or for a high figure of merit, lattice thermal conductivity (κ_l) must be low. At 300 K, lattice thermal conductivity of unstrained LaBrI monolayer was found to be ~5.245 W/m K, which further decreases to 0.059 W/m K with 10% strain. Interestingly, computed lattice thermal conductivity at higher temperature is significantly low (<1.0 W/m K) for LaBrI, as presented in Table II.

As depicted from Fig. 8 for unstrained system, with the increase in temperature from 600 to 800 K, thermal conductivity

TABLE II. Lattice thermal conductivity computed using phono3py at 600 and 800 K.

		Thermal conductivity (W/mK)	
S. No.	Strain %	600 K	800 K
1	0	2.604	1.951
2	4	1.241	0.930
3	8	0.428	0.322
4	10	0.029	0.021

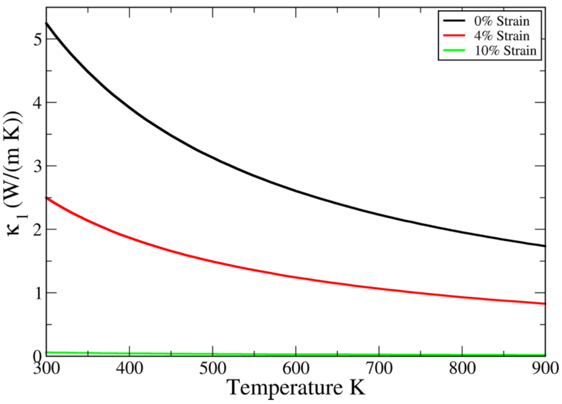

FIG. 8. Variation of phononic part of thermal conductivity with temperature at different strain.

decreases from ∼2.604 to ∼1.951 W/m K, although application of 4% strain slightly decreases the κ_l to ∼0.930 W/m K at 800 K. We noticed a decrease in the lattice thermal conductivity with steady increase in the tensile strain. The decrease in lattice thermal conductivity may be related to increased anharmonic interactions with increase in volume, leading to frequent scattering [77,78]. Therefore, we can infer that low thermal conductivity at higher temperature might result in higher *ZT* of this monolayer.

4. *Thermoelectric figure of merit (ZT)*

We further computed the dimensionless figure of merit to predict the thermoelectric efficiency by employing the above discussed transport coefficients. Since the electronic transport coefficients are computed within constant relaxation time approximation, we have considered two constant values of relaxation to further predict the *ZT*. Considering constant values of $\tau = 10^{-13}$ and 10^{-14} s, we have computed *ZT* as shown in Fig. 9. Computed results with $\tau = 10^{-14}$ s for unstrained LaBrI have a $ZT < 1$ whereas $\tau = 10^{-13}$ s results in a $ZT = 1.24$ at 800 K. Variations of temperature and strain have significant effect on *ZT*. For $\tau = 10^{-13}$ s, *ZT* enhanced from ∼0.85 for unstrained LaBrI to ∼1.27 with 4% strain for down spin with *n*-type doping at 600 K. At 800 K, with 4% strain we obtained the highest *ZT* of ∼1.84 for down spin with *n*-type doping. Computed *ZT* with higher strain has a slowly decreased *ZT* of 1.74 for 8% strain and 1.80 for 10% strain. Similarly, for $\tau = 10^{-14}$ s the *ZT* value at 800 K is 1.72 and at 600 K it becomes 1.68 with 10% strain. Thus, *ZT* calculated with $\tau = 10^{-13}$ s clearly signifies higher *ZT* with 4% strain, which signifies strain-enhanced thermoelectric figure of merit.

Moreover, the studied Janus monolayer LaBrI exhibits higher *ZT* values which are prominent for potential thermoelectric materials.

IV. CONCLUSIONS

We have systematically investigated the structural parameters of 2D Janus ferrovalley LaBrI material. Phonon dispersion curves at different strains revealed this material to be dynamically stable up to 10% strain. The calculated electronic band structure signifies LaBrI to be an indirect band-gap (0.51 eV) ferromagnetic material with a magnetic moment of 1.0 μ_B. Band gap with spin-up and spin-down charge carriers can be effectively modulated by biaxial tensile strain and it has a crucial impact on the thermoelectric

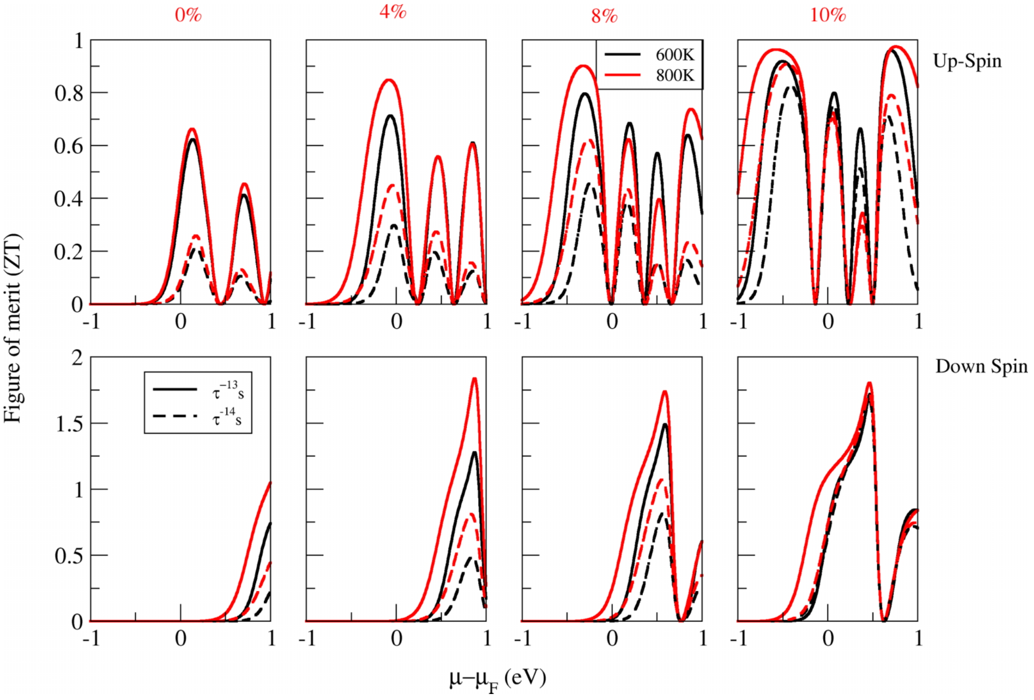

FIG. 9. *ZT* as a function of chemical potential in different temperature regions with two values of relaxation times, solid lines representing $\tau = 10^{-13}$ s and dashed lines representing $\tau = 10^{-14}$ s.

transport properties. Computed thermoelectric coefficients suggest that this material can have a high power factor with n-type and p-type dopings and low lattice thermal conductivities of $\sim 0.93\,\mathrm{W/m\,K}$ that results in a high $ZT \sim 1.84$ at 800 K at 4% strain. Thus, computed $ZT > 1$ for strained monolayer is comparable to the commercially used TE materials such as $\mathrm{Bi_2Te_3}$, oxides, and sulfides. Such high value of ZT indicates the potential of this monolayer for thermoelectric applications.

ACKNOWLEDGMENTS

We would like to acknowledge the fellowship and computational resources provided by the Indian Statistical Institute, Kolkata, which have been helpful during this research. Also, we would like to acknowledge the developers of Quantum Espresso for providing free open-source codes. R.K.B. acknowledges Science and Engineering Research Board (Grant No. EEQ/2022/000325) for the financial support.

---

[1] T.-Z. Ang, M. Salem, M. Kamarol, H. S. Das, M. A. Nazari, and N. Prabaharan, A comprehensive study of renewable energy sources: Classifications, challenges, and suggestions, Energy Strategy Rev. **43**, 100939 (2022).

[2] Z. Wehbi, R. Taher, J. Faraj, C. Castelain, and M. Khaled, Hybrid thermoelectric generators-renewable energy systems: A short review on recent developments, Energy Rep. **8**, 1361 (2022).

[3] M. Sasidharan, M. F. M. Sabri, S. F. W. M. Hatta, and S. Ibrahim, A review on the progress and development of thermoelectric air conditioning system, Int. J. Green Energy **21**, 283 (2024).

[4] R. Maleki, M. Asadnia, and A. Razmjou, Artificial intelligence-based material discovery for clean energy future, Adv. Intell. Syst. **4**, 2200073 (2022).

[5] K. Ma, L. Xu, A. M. Abed, D. H. Elkamchouchi, M. A. Khadimallah, H. E. Ali, H. Algarni, and H. Assilzadeh, An artificial intelligence approach study for assessing hydrogen energy materials for energy saving in building, Sustainable Energy Technol. Assess. **56**, 103052 (2023).

[6] M. D. A. Albert, K. O. Bennett, C. A. Adams, and J. G. Gluyas, Waste heat mapping: A UK study, Renewable Sustainable Energy Rev. **160**, 112230 (2022).

[7] O. Farhat, J. Faraj, F. Hachem, C. Castelain, and M. Khaled, A recent review on waste heat recovery methodologies and applications: Comprehensive review, critical analysis, and potential recommendations, Cleaner Eng. Technol. **6**, 100387 (2022).

[8] R. Nandhini, B. Sivaprakash, and N. Rajamohan, Waste heat recovery at low temperature from heat pumps, power cycles and integrated systems–Review on system performance and environmental perspectives, Sustainable Energy Technol. Assess. **52**, 102214 (2022).

[9] Z. Tian, Z. Qi, W. Gan, M. Tian, and W. Gao, A novel negative carbon-emission, cooling, and power generation system based on combined LNG regasification and waste heat recovery: Energy, exergy, economic, environmental (4E) evaluations, Energy **257**, 124528 (2022).

[10] A. Patel, Advancements in heat exchanger design for waste heat recovery in industrial processes, World J. Adv. Res. Rev. (WJARR) **19**, 137 (2023).

[11] A. Kumari, A. Nag, and J. Kumar, *Ab-initio* study of halogen inter-substituted perovskite cesium leads halides for photovoltaic applications, J. Phys. Chem. Solids **161**, 110430 (2022).

[12] A. G. Olabi, M. Al-Murisi, H. M. Maghrabie, B. A. A. Yousef, E. T. Sayed, A. H. Alami, and M. A. Abdelkareem, Potential applications of thermoelectric generators (TEGs) in various waste heat recovery systems, Int. J. Thermofluids **16**, 100249 (2022).

[13] M. Ge, Z. Li, Y. Zhao, Z. Xuan, Y. Li, and Y. Zhao, Experimental study of thermoelectric generator with different numbers of modules for waste heat recovery, Appl. Energy **322**, 119523 (2022).

[14] A. O. Ochieng, T. F. Megahed, S. Ookawara, and H. Hassan, Comprehensive review in waste heat recovery in different thermal energy-consuming processes using thermoelectric generators for electrical power generation, Process Saf. Environ. Prot. **162**, 134 (2022).

[15] X. Ma, S. Hu, W. Hu, Y. Luo, and H. Cheng, Experimental investigation of waste heat recovery of thermoelectric generators with temperature gradient, Int. J. Heat Mass Transfer **185**, 122342 (2022).

[16] N. V. Burnete, F. Mariasiu, C. Depcik, I. Barabas, and D. Moldovanu, Review of thermoelectric generation for internal combustion engine waste heat recovery, Prog. Energy Combust. Sci. **91**, 101009 (2022).

[17] S. Zhu, Z. Fan, B. Feng, R. Shi, Z. Jiang, Y. Peng, J. Gao, L. Miao, and K. Koumoto, Review on wearable thermoelectric generators: From devices to applications, Energies **15**, 3375 (2022).

[18] Y. Liu, J.-R. Riba, M. Moreno-Eguilaz, and J. Sanllehi, Application of thermoelectric generators for low temperature gradient energy harvesting, Appl. Sci. **13**, 2603 (2023).

[19] S. Newby, W. Mirihanage, and A. Fernando, Recent advancements in thermoelectric generators for smart textile application, Mater. Today Commun. **33**, 104585 (2022).

[20] M. Jabri, S. Masoumi, F. Sajadirad, R. P. West, and A. Pakdel, Thermoelectric energy conversion in buildings, Mater. Today Energy **32**, 101257 (2023).

[21] M. A. Zoui, S. Bentouba, J. G. Stocholm, and M. Bourouis, A review on thermoelectric generators: Progress and applications, Energies **13**, 3606 (2020).

[22] A. Nag, Y. Gupta, and J. Kumar, Spin-polarized linear dispersions, lattice dynamics and transport properties of quaternary Heusler alloys (LiMgXSb), Mater. Chem. Phys. **297**, 127373 (2023).

[23] Q. Ma, H. Fang, and M. Zhang, Theoretical analysis and design optimization of thermoelectric generator, Appl. Therm. Eng. **127**, 758 (2017).

[24] R. McCarty, Thermoelectric power generator design for maximum power: It's all about ZT, J. Electron. Mater. **42**, 1504 (2013).

[25] G. Pennelli, E. Dimaggio, and M. Macucci, Electrical and thermal optimization of energy-conversion systems based on thermoelectric generators, Energy **240**, 122494 (2022).

[26] R. Tuley and K. Simpson, ZT optimization: An application focus, Materials **10**, 309 (2017).

[27] Z. H. Hou, X. Qian, Q. J. Cui, S. F. Wang, and L. D. Zhao, Strategies to advance thermoelectric performance of PbSe and PbS materials, Rare Metals **43**, 4099 (2024).

[28] M. Wolf, R. Hinterding, and A. Feldhoff, High power factors vs. high zT- A review of thermoelectric materials for high-temperature application, Entropy **21**, 1058 (2019).

[29] Z. Ma, J. Wei, P. Song, M. Zhang, L. Yang, J. Ma, W. Liu, F. Yang, and X. Wang, Review of experimental approaches for improving ZT of thermoelectric materials, Mater. Sci. Semicond. Process. **121**, 105303 (2021).

[30] M. N. Hasan, H. Wahid, N. Nayan, and M. S. M. Ali, Inorganic thermoelectric materials: A review, Int. J. Energy Res. **44**, 6170 (2020).

[31] W.-D. Liu, D.-Z. Wang, Q. Liu, W. Zhou, Z. Shao, and Z.-G. Chen, High-performance GeTe-based thermoelectrics: From materials to devices, Adv. Energy Mater. **10**, 2000367 (2020).

[32] B. Cai, H. Hu, H.-L. Zhuang, and J.-F. Li, Promising materials for thermoelectric applications, J. Alloys Compd. **806**, 471 (2019).

[33] S. Sakane, T. Ishibe, T. Taniguchi, N. Naruse, Y. Mera, T. Fujita, M. M. Alam, K. Sawano, N. Mori, and Y. Nakamura, Thermoelectric power factor enhancement based on carrier transport physics in ultimately phonon-controlled Si nanostructures, Mater. Today Energy **13**, 56 (2019).

[34] R. Xu, L. Huang, J. Zhang, D. Li, J. Liu, J. Liu, J. Fang, M. Wang, and G. Tang, Nanostructured SnSe integrated with Se quantum dots with ultrahigh power factor and thermoelectric performance from magnetic field-assisted hydrothermal synthesis, J. Mater. Chem. A **7**, 15757 (2019).

[35] P. P. Murmu, V. Karthik, Z. Liu, V. Jovic, T. Mori, W. L. Yang, K. E. Smith, and J. V. Kennedy, Influence of carrier density and energy barrier scattering on a high Seebeck coefficient and power factor in transparent thermoelectric copper iodide, ACS Appl. Energy Mater. **3**, 10037 (2020).

[36] Z. Liu, X. Meng, D. Qin, B. Cui, H. Wu, Y. Zhang, S. J. Pennycook, W. Cai, and J. Sui, New insights into the role of dislocation engineering in N-type filled skutterudite $CoSb_3$, J. Mater. Chem. C **7**, 13622 (2019).

[37] X. Guan, W. Feng, X. Wang, R. Venkatesh, and J. Ouyang, Significant enhancement in the Seebeck coefficient and power factor of p-type poly (3, 4-ethylenedioxythiophene): Poly (styrenesulfonate) through the incorporation of n-type MXene, ACS Appl. Mater. Interfaces **12**, 13013 (2020).

[38] K. Tolborg and B. B. Iversen, Chemical bonding origin of the thermoelectric power factor in half-Heusler semiconductors, Chem. Mater. **33**, 5308 (2021).

[39] M. T. Dylla, J. J. Kuo, I. Witting, and G. J. Snyder, Grain boundary engineering nanostructured $SrTiO_3$ for thermoelectric applications, Adv. Mater. Interfaces **6**, 1900222 (2019).

[40] T. Zhao, H. Zhu, B. Zhang, S. Zheng, N. Li, G. Wang, G. Wang, X. Lu, and X. Zhou, High thermoelectric performance of tellurium-free n-type $AgBi_{1-x}Sb_xSe_2$ with stable cubic structure enabled by entropy engineering, Acta Mater. **220**, 117291 (2021).

[41] J. Wei, L. Yang, Z. Ma, P. Song, M. Zhang, J. Ma, F. Yang, and X. Wang, Review of current high-ZT thermoelectric materials, J. Mater. Sci. **55**, 12642 (2020).

[42] A. He, S. K. Bux, Y. Hu, D. Uhl, L. Li, D. Donadio, and S. M. Kauzlarich, Structural complexity and high thermoelectric performance of the Zintl phase: $Yb_{21}Mn_4Sb_{18}$, Chem. Mater. **31**, 8076 (2019).

[43] X. Zhang, Y. Guo, Z. Zhou, Y. Li, Y. Chen, and J. Wang, A general strategy for designing two-dimensional high-efficiency layered thermoelectric materials, Energy Environ. Sci. **14**, 4059 (2021).

[44] H. Lai, Y. Peng, J. Gao, M. Kurosawa, O. Nakatsuka, T. Takeuchi, and L. Miao, Silicon-based low-dimensional materials for thermal conductivity suppression: Recent advances and new strategies to high thermoelectric efficiency, Jpn. J. Appl. Phys. **60**, SA0803 (2020).

[45] Y.-K. Jung, I. T. Han, Y. C. Kim, and A. Walsh, Prediction of high thermoelectric performance in the low-dimensional metal halide $Cs_3Cu_2I_5$, npj Comput. Mater. **7**, 51 (2021).

[46] S.-Z. Huang, Q.-Y. Feng, B.-Y. Wang, H.-D. Yang, B. Li, X. Xiang, X.-T. Zu, and H.-X. Deng, Valley degeneracy-enhanced thermoelectric performance in In-based FeOCl-type monolayers, ACS Appl. Energy Mater. **5**, 13042 (2022).

[47] Z. Guo, Q. Zhang, H. Wang, X. Tan, F. Shi, C. Xiong, N. Man, H. Hu, G. Liu, and J. Jiang, Bi–Zn codoping in GeTe synergistically enhances band convergence and phonon scattering for high thermoelectric performance, J. Mater. Chem. A **8**, 21642 (2020).

[48] P.-A. Zong, J. Liang, P. Zhang, C. Wan, Y. Wang, and K. Koumoto, Graphene-based thermoelectrics, ACS Appl. Energy Mater. **3**, 2224 (2020).

[49] M. Markov and M. Zebarjadi, Thermoelectric transport in graphene and 2D layered materials, Nanoscale Microscale Thermophys. Eng. **23**, 117 (2019).

[50] X.-L. Zhu, H. Yang, W.-X. Zhou, B. Wang, N. Xu, and G. Xie, KAgX (X = S, Se): High-performance layered thermoelectric materials for medium-temperature applications, ACS Appl. Mater. Interfaces **12**, 36102 (2020).

[51] X. Zhang, C. Liu, Y. Tao, Y. Li, Y. Guo, Y. Chen, X. C. Zeng, and J. Wang, High ZT 2D thermoelectrics by design: Strong interlayer vibration and complete band-extrema alignment, Adv. Funct. Mater. **30**, 2001200 (2020).

[52] S. Sarikurt, T. Kocabaş, and C. Sevik, High-throughput computational screening of 2D materials for thermoelectrics, J. Mater. Chem. A **8**, 19674 (2020).

[53] Z. Zhu, X. Cai, S. Yi, J. Chen, Y. Dai, C. Niu, Z. Guo, M. Xie, F. Liu, J.-H. Cho, Y. Jia, and Z. Zhang, Multivalency-driven formation of Te-based monolayer materials: A combined first-principles and experimental study, Phys. Rev. Lett. **119**, 106101 (2017).

[54] B. Zhu, Q. Chen, S. Jiang, M. Holt, W. Zhu, D. Akinwande, and L. Tao, Thermoelectric effect and devices on IVA and VA Xenes, InfoMat **3**, 271 (2021).

[55] J. Yuan, G. Liu, Y. Xin, X. Wang, Y. Liu, X. Han, S. Fu, Z. Man, F. Xing, and F. Zhang, Synthetic 2D tellurium nanosheets with intense TE wave polarization absorption by employing the PVD method, J. Nanopart. Res. **24**, 130 (2022).

[56] J. Kim, S. Youn, J. Bang, H. Moon, W. Jang, J. W. Roh, D. H. Kim, J. Chang, and W. Lee, Experimental verification of semimetallic band structure in $PtSe_2$ via thermoelectric power measurements, Appl. Phys. Lett. **120**, 043103 (2022).

[57] X. Gu and R. Yang, Phonon transport in single-layer transition metal dichalcogenides: A first-principles study, Appl. Phys. Lett. **105**, 131903 (2014).

[58] R. Li, Y. Cheng, and W. Huang, Recent progress of Janus 2D transition metal chalcogenides: From theory to experiments, Small **14**, 1802091 (2018).

[59] A. Kumari, A. Nag, and J. Kumar, Strain engineering and thermoelectric performance of Janus monolayers of titanium dichalcogenides: A DFT study, Comput. Mater. Sci. **218**, 111925 (2023).

[60] A. Patel, D. Singh, Y. Sonvane, P. B. Thakor, and R. Ahuja, High thermoelectric performance in two-dimensional Janus monolayer material WS-X (X = Se and Te), ACS Appl. Mater. Interfaces **12**, 46212 (2020).

[61] S.-Z. Huang, C.-G. Fang, Q.-Y. Feng, B.-Y. Wang, H.-D. Yang, B. Li, X. Xiang, X.-T. Zu, and H.-X. Deng, Strain tunable thermoelectric material: Janus ZrSSe monolayer, Langmuir **39**, 2719 (2023).

[62] W.-L. Tao, J.-Q. Lan, C.-E. Hu, Y. Cheng, J. Zhu, and H.-Y. Geng, Thermoelectric properties of Janus MXY (M = Pd, Pt; X, Y = S, Se, Te) transition-metal dichalcogenide monolayers from first principles, J. Appl. Phys. **127**, 035101 (2020).

[63] S. Saini, A. Shrivastava, A. Dixit, and S. Singh, Ultra-low lattice thermal conductivity and high figure of merit for Janus MoSeTe monolayer: A peerless material for high temperature regime thermoelectric devices, J. Mater. Sci. **57**, 7012 (2022).

[64] S. Sattar, M. F. Islam, and C. M. Canali, Monolayer Mn X and Janus X Mn Y (X, Y = S, Se, Te): A family of two-dimensional antiferromagnetic semiconductors, Phys. Rev. B **106**, 085410 (2022).

[65] D. Wu, Z. Zhuo, H. Lv, and X. Wu, Two-dimensional $Cr_2X_3S_3$ (X = Br, I) Janus semiconductor with intrinsic room-temperature magnetism, J. Phys. Chem. Lett. **12**, 2905 (2021).

[66] P. Jiang, L. Kang, Y.-L. Li, X. Zheng, Z. Zeng, and S. Sanvito, Prediction of the two-dimensional Janus ferrovalley material LaBrI, Phys. Rev. B **104**, 035430 (2021).

[67] R. Chaurasiya, S. Tyagi, N. Singh, S. Auluck, and A. Dixit, Enhancing thermoelectric properties of Janus WSSe monolayer by inducing strain mediated valley degeneracy, J. Alloys Compd. **855**, 157304 (2021).

[68] P. Giannozzi, S. Baroni, N. Bonini, M. Calandra, R. Car, C. Cavazzoni, D. Ceresoli *et al.*, QUANTUM ESPRESSO: A modular and open-source software project for quantum simulations of materials, J. Phys.: Condens. Matter **21**, 395502 (2009).

[69] J. P. Perdew, K. Burke, and M. Ernzerhof, Generalized gradient approximation made simple, Phys. Rev. Lett. **77**, 3865 (1996).

[70] G. K. H. Madsen and D. J. Singh, BoltzTraP. A code for calculating band-structure dependent quantities, Comput. Phys. Commun. **175**, 67 (2006).

[71] W. Li, J. Carrete, N. A. Katcho, and N. Mingo, Shengbte: A solver of the Boltzmann transport equation for phonons, Comput. Phys. Commun. **185**, 1747 (2014).

[72] Y. Zhang, First-principles Debye–Callaway approach to lattice thermal conductivity, J. Materiomics **2**, 237 (2016).

[73] A. Togo, L. Chaput, and I. Tanaka, Distributions of phonon lifetimes in Brillouin zones, Phys. Rev. B **91**, 094306 (2015).

[74] See Supplemental Material at http://link.aps.org/supplemental/10.1103/PhysRevB.111.155433 for thermal conductivity convergence with q-mesh size and coordinates of high symmetry path.

[75] A. Nag and J. Kumar, Dirac dispersions, lattice dynamics and thermoelectric properties of quaternary Heusler alloys LiMgXY (X = Pt, Pd, Au; Y = Sb, Sn), Mater. Today Commun. **31**, 103400 (2022).

[76] A. Nag, A. Kumari, and J. Kumar, Revisiting Wiedemann-Franz law through Boltzmann transport equations and ab-initio density functional theory, AIP Conf. Proc. **1953**, 030163 (2018).

[77] Z. Xu, Q. Xia, and G. Gao, A strain-induced considerable decrease of lattice thermal conductivity in 2D KAgSe with Coulomb interaction, Phys. Chem. Chem. Phys. **24**, 24917 (2022).

[78] C. Kwon, Y. Xia, F. Zhou, and B. Han, Dominant effect of anharmonicity on the equation of state and thermal conductivity of MgO under extreme conditions, Phys. Rev. B **102**, 184309 (2020).